

Near-field effects on coherent anti-Stokes Raman scattering microscopy imaging

Cheng Liu, Zhiwei Huang*, Fake Lu, Wei Zheng, Dietmar W. Huttmacher, and
Colin Sheppard

Bioimaging Laboratory, Department of Bioengineering, Faculty of Engineering,
National University of Singapore, Singapore 117576
biehzw@nus.edu.sg

Abstract: We introduce a numerical approach, the finite-difference time-domain (FDTD) method, to study the near-field effects on coherent anti-Stokes Raman scattering (CARS) microscopy on nanoparticles. Changes of the induced nonlinear polarization, scattering patterns, and polarization properties against different diameters of spherical nanoparticles are calculated and discussed in detail. The results show that due to near-field effects, the induced nonlinear polarization is significantly enhanced at the water-particle interface, with 1.5-fold increase in intensity compared to that inside the particles, and the near-field enhancement increases with decreasing diameters of nanoparticles. The enhanced scattering dominates over the scattering contribution from the particles when the nanoparticle size decreases down to the scale of less than a half wavelength of excitation light. Further studies show that near-field effects make the induced perpendicular polarization of CARS signals being strictly confined within the nanoparticles and the particle-water interface, and this perpendicular polarization component could contribute approximately 20% to the backward scattering. The ratio values of the perpendicular polarization component to the total CARS signals from nanoparticles sizing from 75 nm to 300 nm in backward scattering are approximately 3 to 5 times higher than those in forward scattering. Therefore, near-field effects can play an important role in CARS imaging. Employing the perpendicular polarization component of CARS signals can significantly improve the contrast of CARS images, and be particularly useful for revealing the fine structures of bio-materials with nano-scale resolutions.

©2007 Optical Society of America

OCIS codes: (180.6900) Three-dimensional microscopy; (190.3970) Microparticle nonlinear optics; (300.6230) Spectroscopy, coherent anti-Stokes Raman scattering;

References and links

1. R. J. H. Clark and R. E. Hester, *Advances in Nonlinear Spectroscopy* (Wiley, New York, 1988).
2. P. D. Maker and R. W. Terhune, "Study of optical effects due to an induced polarization third order in the electric field strength," *Phys. Rev.* **137**, A801 (1965).
3. Y. R. Shen, *The Principles of Nonlinear Optics* (Wiley, New York, 1984).
4. J. X. Cheng and X. S. Xie, "Coherent anti-Stokes scattering microscopy: instrumentation, theory, and application," *J. Phys. Chem. B* **108**, 827 (2004).
5. J. X. Cheng, A. Volkmer and X. S. Xie, "Theoretical and experimental characterization of coherent anti-Stokes Raman scattering microscopy," *J. Opt. Soc. Am. B* **19**, 1363 (2002).
6. H. Wang, Y. Fu, P. Zickmund, R. Shi and J. X. Cheng, "Coherent anti-Stokes Raman scattering imaging of axonal myelin in live spinal tissues," *Biophys. J.* **89**, 581 (2005).
7. E. O. Potma, C. L. Evans and X. S. Xie, "Heterodyne coherent anti-Stokes Raman scattering (CARS) imaging," *Opt. Lett.* **31**, 241 (2006).
8. J. P. Ogilvie, E. Beaufort, A. Alexandrou and M. Joffre, "Fourier-transform coherent anti-Stokes Raman scattering microscopy," *Opt. Lett.* **31**, 480 (2006).
9. D. Oron, N. Dudovich and Y. Silberberg, "Single-pulse phase-contrast nonlinear Raman spectroscopy," *Phys. Rev. Lett.* **89**, 273001 (2002).

10. E. R. Andresen and H. N. Paulsen, V. Birkedal, J. Thøgersen and S. R. Keiding, "Broadband multiplex coherent anti-Stokes Raman scattering microscopy employing photonic-crystal fibers," *J. Opt. Am. B* **22**, 1934 (2005).
11. J. X. Cheng and X. S. Xie, "Green's function formulation for third-harmonic generation microscopy," *J. Opt. Soc. Am. B* **19**, 1604 (2002).
12. C. Liu and S. H. Park, "Anisotropy of near-field speckle patterns," *Opt. Lett.* **30**, 1602 (2005).
13. T. Ichimura, N. Hayazawa, M. Hashimoto, Y. Inouye and S. Kawata, "Tip-enhanced coherent anti-Stokes Raman scattering for vibrational nano-imaging," *Phys. Rev. Lett.* **92**, 220801 (2004).
14. Yee K.S. "Numerical solution of initial boundary value problem involving Maxwell equations in isotropic media," *IEEE Trans. Antennas Propagat.* **14**, 302 (1966).
15. A. Taflove, *Computational Electrodynamics: The Finite-Difference Time-Domain Method* (Artech House, Boston, 1995).
16. R. W. Boyd, *Nonlinear Optics* (Academic, Boston, Mass., 1992).
17. S. Mukamel, *Principles of Nonlinear Optical Spectroscopy* (Oxford University Press, New York, 1995).
18. S. Y. Hasegawa, N. Aoyama, A. Futamata and T. Uchiyama, "Optical tunneling effect calculation of a solid immersion lens for use in optical disk memory," *Appl. Opt.* **38**, 2297 (1999).
19. K. Takeda, Y. Ito and C. Munakata, "Simultaneous measurement of size and refractive index of a fine particle in flowing liquid," *Meas. Sci. Technol.* **3**, 27 (1992).
20. M. Born and E. Wolf, *Principles of Optics: Electromagnetic Theory of Propagation, Interference and Diffraction of Light (7th Edition)* (Cambridge University Press, New York, 2002).
21. H. Lotem, R. T. Lynch and N. Blombergen, "Interference between Raman resonances in four-wave difference mixing," *Phys. Rev.* **126**, 1977 (1962).
22. B. Richards and E. Wolf, "Electromagnetic diffraction in optical systems II: Structure of the image field in an aplanatic system," *Proc. Roy. Soc. A* **253**, 358 (1959).
23. L. Novotny and B. Hecht, *Principles of Nano-optics* (Cambridge University Press, New York, 2006).
24. T. Wilson and J. B. Tan, "Finite sized coherent and incoherent detectors in confocal microscopy," *J. Microsc.* **182**, 61 (1995).

1. Introduction

Coherent anti-Stokes Raman scattering (CARS) is a third-order nonlinear optical process involving in interactions between a pump beam of frequency ω_p , a Stokes beam of frequency ω_s , and a CARS signal at the anti-Stokes frequency of $\omega_{as}=2\omega_p-\omega_s$ generated in the phase matching direction [1]. The vibrational contrast in CARS microscopy is created when the frequency difference $\omega_p-\omega_s$ between the pump and the Stokes beams is tuned to be resonant with a Raman-active molecular vibration of samples. CARS signal is free of autofluorescence background due to the anti-Stokes shifting, and is more efficient than conventional Raman scattering due to stimulated generation of signal. Recently, CARS technique has received great interest in imaging live cells [2-10], owing to its outstanding abilities of providing both the biochemical compositions and biomolecular structural information about biosamples in aqueous environments without fluorescence probes, high sensitivity as well as intrinsic three-dimensional optical sectioning ability with high spatial and spectral resolutions.

It is known that the intensity of CARS signal generated from a given sample is proportional to the product of the density of molecules, the square of the intensity of the pump beam, and the intensity of the Stokes beam. As such, under a spatially uniform illumination condition, the CARS technique can be used to determine the density of the molecules and the molecular structures in samples. This is the fundamental assumption in most wide-field or far-field studies on CARS microscopy [11]. However, the resonant Raman signal, in fact, is generated only from specific chemical bonds of molecules in the samples, and the CARS signal is determined by the local excitation light fields surrounding the chemical bonds, rather than just simply being determined by the illumination light fields. In the cases of CARS studies on small live cells or organelles, if the physical size of targets of interest (e.g., mitochondria, membranes) is equivalent to or even smaller than the wavelength of excitation light used, it is expected that the evanescent waves generated due to the near-field effects could dominate the local light fields within the molecule, and vary with a number of near-field factors such as the refractive index mismatch, edge effect, surface roughness, and etc [12, 13]. That is, the spatially uniform illumination light field may not be the only excitation light source for generating the nonlinear CARS signals. For a given molecule, the induced

nonlinear polarization component depends not only on the nonlinear coefficient and the illumination light fields, but also on the local light field. Hence, the near-field effects should be taken into account in CARS microscopy particularly on nano-molecular imaging.

In this study, we applied an advanced and powerful numerical approach, the finite-difference time-domain (FDTD) method [14], to study the influences of near-field effects on CARS generation and light propagation in spherical nanoparticles, and to evaluate the possibility of using the near-field effects to improve the image contrast in CARS microscopy imaging.

2. Finite-difference time-domain (FDTD) method for simulations

Light propagation in turbid media (e.g., biotissue) can be determined, in principle, by solving Maxwell equations [3]; however, due to the complexities of boundary conditions, it is impossible to obtain explicit solutions to Maxwell equations for most practical cases. Recent years, the numerical technique, the finite difference time domain (FDTD) method, which bases on a leapfrog strategy [14] to directly provide numerical solutions to the Maxwell equations with high precisions, has become a powerful means for local fields calculation in both optics and photonics [15]. In FDTD simulation, the space is discretized into uniform or un-uniform grids with intervals to be much smaller than the wavelength of excitation light used, assuming that the refractive index and the electromagnetic field within each small grid are uniform. When the grid is sufficiently small, both the temporal and spatial differences in Maxwell equations can be approximated with finite differences, thus the electric field at a given time and position $E(t_n, x)$ can be determined using the electric field of the position at previous time $E(t_{n-2}, x)$ and the spatial finite-difference of the magnetic fields of surrounding grids at time t_{n-1} . The magnetic field $H(t_{n-2}, x)$ can be obtained using the $H(t_{n-1}, x)$ and the finite-difference of the electric field of surrounding grids at time t_n . After a number of iterations on electric and magnetic fields, the calculated electromagnetic field will converge to an explicit value anticipated by Maxwell equations.

The generation and propagation of the CARS field in a homogeneous and isotropic medium are governed by the wave equation [16, 17].

$$\nabla \times \nabla \times \mathbf{E}(\mathbf{r}, t) + \frac{n^2}{c^2} \frac{\partial^2 \mathbf{E}(\mathbf{r}, t)}{\partial t^2} = -\frac{4\pi}{c^2} \frac{\partial^2 \mathbf{P}^{(3)}(\mathbf{r}, t)}{\partial t^2} \quad (1)$$

where $\mathbf{P}^{(3)}(\mathbf{r}, t)$ is the third-order nonlinear polarization, n is the refractive index of the medium for the signal field, and c is the velocity of light in vacuum. The third-order polarization at the anti-Stokes frequency of $\omega_{as} = 2\omega_p - \omega_s$ can be written as

$$P_i^{(3)}(\mathbf{r}, \omega_{as}, t) = 3 \sum_{jkl} \chi_{ijkl}^{(3)} E_j^p(\mathbf{r}, \omega_p, t) E_k^p(\mathbf{r}, \omega_p, t) E_l^{s*}(\mathbf{r}, \omega_s, t) \quad (2)$$

where $\chi_{ijkl}^{(3)}$ is the third-order nonlinear coefficient of an isotropic medium; $E_j^p(\mathbf{r}, \omega_p, t)$, $E_k^p(\mathbf{r}, \omega_p, t)$, and $E_l^{s*}(\mathbf{r}, \omega_s, t)$ are the time-dependant amplitudes of the pump and the Stokes beams in j , k , and l directions, respectively. If the distributions of the pump and the Stokes light fields, and the third-order nonlinear coefficient are known, the third-order nonlinear polarization at different directions can be determined using Eq. (2), and then the CARS distribution could be derived by solving Eq. (1). However, when the near-field effects are taken into account, such as the presence of non-propagating evanescent waves, it is difficult to directly determine the excitation light fields to obtain the explicit solutions of Eq. (1) due to the complex boundary conditions introduced by the near-field effects. With the advantage of without the need to consider the boundary conditions, the FDTD method is employed in this study to simulate the CARS generation and propagation, by solving the Maxwell equations numerically with leapfrog approach.

When there is no free electric charge and current source in the medium of interest, the Maxwell equations are written as

$$\begin{cases} \nabla \times H = \frac{\partial D}{\partial t} \\ \nabla \times E = -\frac{\partial B}{\partial t} \end{cases} \quad (3)$$

where H, D, E, and B stand for magnetic field, electric displacement, electric field, and magnetic flux density, respectively. In FDTD simulations, Eq. (3) is discretized with standard staggered grids in temporal and spatial domains. The discretized equations for electric fields in the FDTD simulator for 3-D coordinates are as follows [14]:

$$\begin{cases} E_x^{n+1}(i+0.5, j, k) = CA(m) \cdot E_x^n(i+0.5, j, k) + CB(m)[(H_z^{n+0.5}(i+0.5, j+0.5, k) - H_z^{n+0.5}(i+0.5, j-0.5, k))/\Delta y \\ \quad - (H_y^{n+0.5}(i+0.5, j, k+0.5) - H_y^{n+0.5}(i+0.5, j, k-0.5))/\Delta z] \\ E_y^{n+1}(i, j+0.5, k) = CA(m) \cdot E_y^n(i, j+0.5, k) + CB(m)[(H_x^{n+0.5}(i, j+0.5, k+0.5) - H_x^{n+0.5}(i, j+0.5, k-0.5))/\Delta z \\ \quad - (H_z^{n+0.5}(i+0.5, j+0.5, k) - H_z^{n+0.5}(i-0.5, j+0.5, k))/\Delta x] \\ E_z^{n+1}(i, j, k+0.5) = CA(m) \cdot E_z^n(i, j, k+0.5) + CB(m)[(H_y^{n+0.5}(i+0.5, j, k+0.5) - H_y^{n+0.5}(i-0.5, j, k+0.5))/\Delta x \\ \quad - (H_x^{n+0.5}(i, j+0.5, k+0.5) - H_x^{n+0.5}(i, j-0.5, k+0.5))/\Delta y] \end{cases} \quad (4)$$

where $CA(m) = [2\epsilon(m) - \sigma(m)\Delta t]/[2\epsilon(m) + \sigma(m)\Delta t]$, $CB(m) = 2\Delta t/[2\epsilon(m) + \sigma(m)\Delta t]$, and m is the index of the discretized cell. The discretized equations for the magnetic fields in the FDTD simulator can also be written similarly to the electric fields above [Eq. (4)]. After a number of times of leapfrog iterations using Eq. (4), the electromagnetic field will converge to a stable value determined by the related boundary conditions. Based on this leapfrog approach in time-domain, FDTD simulator will determine not only the steady-state parameters (e.g., intensity distribution of light fields, phase and polarization of the localized light fields), but also the temporal evolution of these parameters against time.

For analysis of CARS signals generation and propagation in nanoparticles, the FDTD method was firstly utilized in this study to determine the local excitation light fields surrounding the scatterers, and then Eq. (2) was used to calculate the induced nonlinear polarizations, and finally the scattering pattern of CARS signals was also calculated by taking the induced nonlinear polarization into account as an additional radiation source for CARS generation.

3. Simulation results

3.1. Geometry and parameters for FDTD simulations

Figure 1(a) shows the schematic diagram of light illuminations on the sample (e.g., nanoparticles) in CARS experiments, whereby both the collinear pump and Stokes light beams are in parallel polarization in x-direction, and tightly focused onto the sample by passing through a water-immersion, high numerical aperture (N.A.) microscope objective. To exam the validity of FDTD simulations, we calculated the spatial distribution of excitation light fields around the focal volume [rectangle in dotted lines in Fig. 1(a)] of the water objective with N.A. of 0.9. In these simulations, the calculation was divided into $400 \times 400 \times 400$ cubic cells of $\lambda_p/40$ (or $\lambda_s/40$) at each step, whereby λ_p (750 nm) is the wavelength of the pump beam, and λ_s (852 nm) is the wavelength of the Stokes beam. The excitation volume of the incident light fields was calculated using the vector formulas [18]. Fig. 1(b) shows the simulated intensity distribution of the excitation light field surrounding the focal volume of the 0.9 N.A. objective in the x-z plane under the condition of without nanoparticles embedded in water. The simulated excitation light field surrounding the focused point has a lateral width of 340 nm in x-direction and an axial length of 1400 nm in z-direction, which are almost the same as the values calculated using the conventional vector formulas [18]. Figure 1(c) displays the corresponding phase distribution of the excitation light field

[Fig. 1(b)] in the x - z plane, depicting that a π - phase change occurs between different orders of the lobes. The above results confirmed the validity of using the FDTD method to study the nonlinear optical process taking place within the excitation volume of the high N.A. objective.

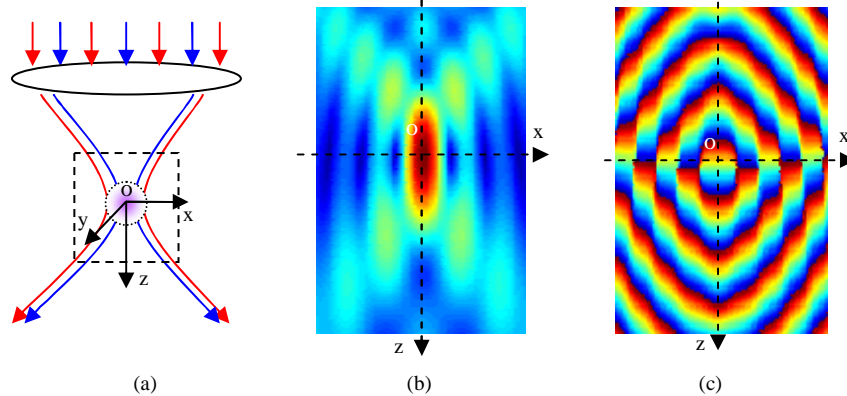


Fig. 1. (a). Schematic diagram of CARS experiments. The collinear pump and Stokes light beams with parallel polarization in x -direction are tightly focused onto the sample located in the focal volume of a high numerical aperture, water-immersion microscope objective; (b) amplitude distribution of the focused light field in water (without nanoparticles) in the x - z plane, and (c) the corresponding phase distribution of the focused light field in the x - z plane. Note that in Fig. 1(a) the red and blue arrows represent the pump and the Stokes light beams, respectively, and the rectangle in dotted lines stands for the excitation volume of light fields for FDTD simulation.

3.2 Distribution of the excitation light fields surrounding nanoparticles

To investigate the near-field effects on CARS signal generation from the scatterers (i.e., nanoparticles), we select spherical polystyrene beads in various diameters ranging from 75 nm to 300 nm as nonlinear scatterers for FDTD simulations. The refractive index of polystyrene beads and the surrounding solvent (i.e., water) are assumed to be 1.59 and 1.33, respectively [19], and other simulation parameters are the same as those mentioned in Section 3.1. If the resonant Raman shift of polystyrene beads is at 1600 cm^{-1} [4], the wavelengths of pump and Stokes light are at 750 nm and 852 nm, respectively, and then the generated CARS signal is at 670 nm.

Figure 2 shows the distribution of the pump light field surrounding the polystyrene bead (200 nm in diameter) located in the focal volume of the objective in the x - z plane (a) and the x - y plane (b), respectively. Figure 2(c) shows the distribution of the amplitude of the electric field E along the x - and y - directions [dotted cross lines in Fig. 2(b)]. One notes that the Stokes light field yields a similar distribution in the nanoparticles as compared to the pump beam (data not shown). In comparison with the light field distribution in the focal volume in water without spherical nanoparticles [blue curve in Fig. 2(c)], the illumination field distribution inside the nanoparticle becomes stronger [red and green curves in Fig. 2(c)], and the light field surrounding the nanoparticle (i.e., at the particle-water interface) is also significantly enhanced [red curve in Fig. 2(c)], especially in the x -direction. This phenomenon can be explained as a result of near-field effect, i.e., the generation of the non-propagating evanescent waves, due to the index mismatch at the nanoparticle-water interface. The refractive index of the nanoparticle $n_{particle}$ is larger than the index of surrounding water n_{water} , the conservation of the electric displacement D at the interface leads to an enhanced electric field in water by a factor of $n_{particle}/n_{water}$ ($1.59/1.33=1.19$) [20]. As the size of the particles is in nano-meter scales, the local field enhancement only takes place within the nano-scales that is much smaller than the excitation light wavelengths. Hence, the enhanced local field is mainly composed by the generated evanescent waves due to the near-field effects [12]. This evanescent field is strictly confined to the vicinity of the particles, which looks like a ‘virtual’

shell surrounding the particles as shown in Fig. 2(c), and therefore, Raman radiation generated from this ‘virtual’ shell is expected to significantly contribute to the CARS signals.

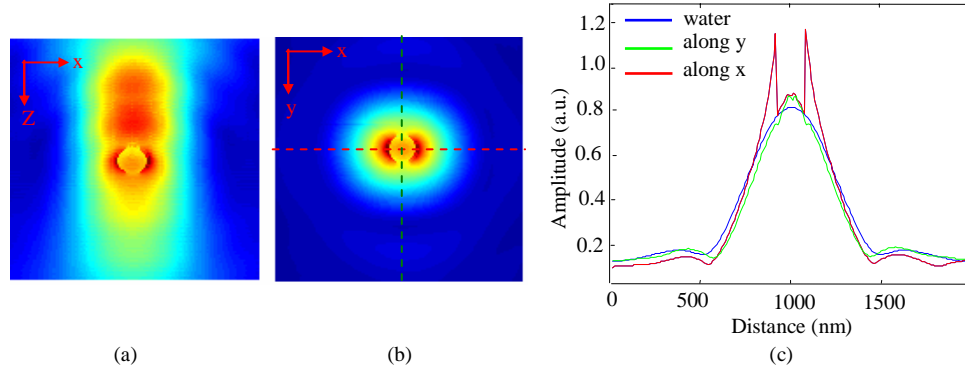


Fig. 2. Distributions of the focal light field surrounding the nanoparticle in the x-z plane (a), and in the x-y plane (b), respectively. (c) Comparison of the intensity profiles of the focal light field in x-direction (red curve) and in y-direction (green curve) with nanoparticles, and the intensity profile of the focal light field distribution in pure water (blue curve).

3.3. Properties of the induced nonlinear polarization

After obtaining the pump and Stokes light field distributions, the induced nonlinear polarization can be computed using Eq. (2). For CARS generation of nanoparticles in water, if we assume that water only has a nonresonant contribution χ_{water}^{NR} , while the scatterer (i.e., nanoparticle) has both resonant and nonresonant components, $\chi_{sca}^{(3)} = \chi_{sca}^{(3)R} + \chi_{sca}^{(3)NR}$; with the nonresonant susceptibilities of both water and scatterers being frequency independent, then the resonant susceptibilities of $\chi_{sca}^{(3)R}$ can be written as [21]:

$$\chi_{sca}^{(3)R}(\omega_{as}) = \chi_{1111}^{(3)R}(\omega_{as}) = \frac{A_R}{\omega_R - (\omega_p - \omega_s) - i\Gamma_R} \quad (5)$$

where Γ_R , ω_R , and A_R are the half-width at the half-maximum of the resonant peak, the resonant vibrational frequency of the Raman mode, and the spontaneous Raman scattering cross-section, respectively.

In our numerical simulations, the nonresonant components of the nonlinear coefficients for both the water and polystyrene beads are estimated using the equation $\chi_{1122}^{(3)NR} = \chi_{1212}^{(3)NR} = \chi_{1221}^{(3)NR} = \chi_{1111}^{(3)NR}/3$. The values of $\Gamma_R = 4.1 \text{ cm}^{-1}$, and $A_R / \chi_{sca}^{(3)NR} = 2.0 \text{ cm}^{-1}$ are chosen in terms of the CARS spectrum of polystyrene bead at the resonant Raman shift ($\omega_R = 1600 \text{ cm}^{-1}$) and the ratio of nonresonant susceptibilities of water to polystyrene beads ($\chi_{water}^{(3)NR} / \chi_{sca}^{(3)NR} = 0.6$) [5]. The resonant polarization vector of the polystyrene bead has an anisotropic mode with $\chi_{1122}^{(3)R} / \chi_{1111}^{(3)R} = 3/4$ [1]. The induced nonlinear cubic polarization is calculated using [1]

$$P_i = 3 \sum_{j,k,l} [(\chi_{1122}^{(3)NR} + \chi_{1122}^{(3)R})(\delta_{ij} + \delta_{kl}) + (\chi_{1221}^{(3)NR} + \chi_{1221}^{(3)R})\delta_{il}\delta_{jk}] E_j^p E_k^s E_l^{s*} \quad (6)$$

where i , j , and k indicate the directions of x , y , and z , respectively. Based on the parameters described above, the susceptibilities of $\chi_{1122}^{(3)NR}$ and $\chi_{1221}^{(3)NR}$ are 0.2 each for water, and 0.333 for polystyrene beads [1].

Figure 3 shows the distributions of the induced nonlinear polarizations (x-component) for nanoparticles with diameters of (a) 75 nm; (b) 125 nm; (c) 200 nm; (d) 250 nm; (e) 300 nm; and (f) 325 nm, respectively. The top two panels in Fig. 3 represent the intensity distributions of the generated polarization in the x-z plane and the x-y plane, respectively. The clear ‘virtual’ shell structures can be found to be surrounding the nanoparticles, due to the

generation of the evanescent waves as elaborated above. One notes that the x - z amplitude distribution of the induced polarization in the first panel of Fig. 3 shows an asymmetric structure in the z direction. This is probably due to the scattering of the incident light from the nanoparticle, resulting in a stronger light field distribution in the upper side of the scatterer than that in the bottom side of the scatterer, although the nanoparticle is located at the center of focal light volume. This asymmetric amplitude distribution becomes more obviously when the particle size increases. The third panel in Fig. 3 shows the corresponding intensity profiles across the particles along the x -direction. It can be observed that the intensity of the induced polarizations inside the nanoparticle increases with the increasing sizes of nanoparticles; while the induced polarization at the particle-water interface is dramatically enhanced compared to that inside the particles or outside the particles, and its intensity increases with the increasing diameters of particles under the condition that the particle's diameter is smaller than the half wavelength of excitation light (the half wavelength of excitation light is 288 nm ($750 \text{ nm}/1.33/2$) in water). But when the diameters of particles are larger than the half wavelength of excitation light (288 nm), the induced polarization outside the particle decreases with the increasing sizes, which probably is due to the weaker near-field effect on the larger particles. On the other hand, the increasing induced polarization inside the larger nanoparticles is due to the fact that the more incident light can be focused onto the larger spherical nanoparticles, leading to a stronger light field distribution than that in smaller nanoparticles (first panel of Fig. 3). The local field enhancement of the induced polarization mainly occurs at the water-particle interface, thus the radiation from the 'virtual' shells located in water mostly comprises the nonresonant Raman components. The bottom panel of Fig. 3 represents the corresponding phase distributions of the induced polarization in the x - z plane, reflecting that the phase changes of the induced polarizations occur at the interface between the particle and the surrounding medium (i.e., water).

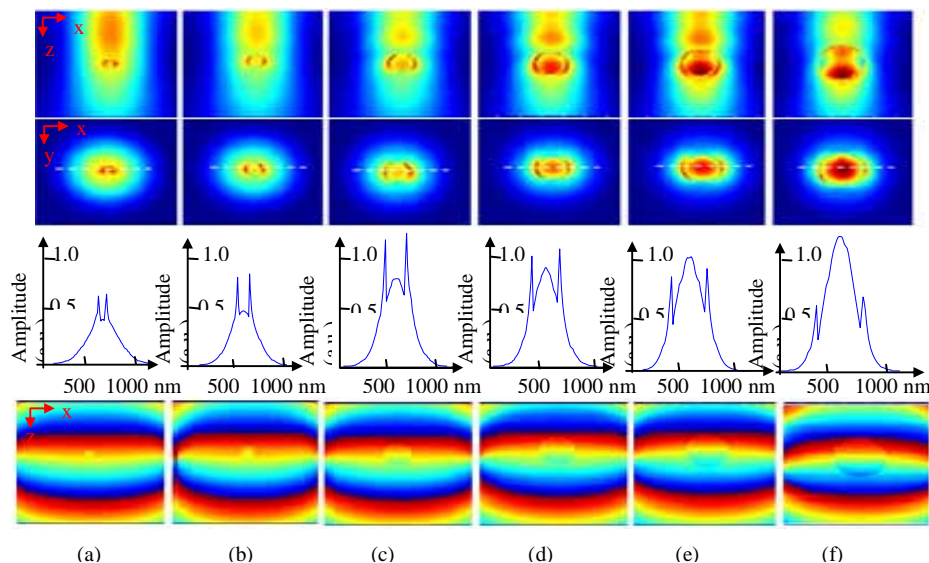


Fig. 3. The induced nonlinear polarizations (x -component) for nanoparticles with diameters of: (a) 75 nm; (b) 125 nm; (c) 200 nm; (d) 250 nm; (e) 300 nm, and (f) 325 nm, respectively. The top two panels represent the amplitude distribution of focal light field in the x - z plane and the x - y plane, respectively. The third panel is the corresponding intensity profiles across the particles along the x -direction as indicated in second panel. The bottom panel represents the corresponding phase distributions of light fields in the x - z plane.

3.4. Scattering of CARS signals from nanoparticles

In CARS microscopy experiments, the detected CARS signals result from the interference of scatterings from both the sample (e.g., nanoparticles) and the surrounding solvent (e.g., water). The former scattering can be used to reveal the physical structure of the sample, while the latter scattering from the water only forms the large background in CARS imaging. Based on the nonlinear-polarization in Section 3.3, the scattering patterns can be readily obtained by simulating the radiation of CARS signals from the polarizations using FDTD.

Figures 4(a)-4(d) show the total scattering patterns of CARS from both the surrounding water and the nanoparticles with diameters of 75 nm, 125 nm, 250 nm, and 325 nm, respectively. The amplitude of the scattering increases with the increasing particle sizes in both the forward and backward directions, however, the forward scattering yields 12~18 folds stronger than that of backward scattering. The simulation results are in accordance with the reports in literature on CARS experiments on cells and tissues [4-7].

Figures 4(e)-4(h) show the scattering patterns of CARS signals from the nanoparticle alone with diameters of 75 nm, 125 nm, 250 nm, and 325 nm, respectively. The forward and backward scatterings also increase with the increasing particle sizes. However, the amplitudes of scatterings from particles [Figs. 4(e)-4(h)] are approximately 30 to 3 times smaller than those of the corresponding total scatterings [Figs. 4(a)-4(d)]. This indicates that most of CARS signals detected from nanoparticles immersed in water (which is similar to the living cell environment) mainly comprise the nonresonant background from water, and thus suppression of the water contribution should be conducted to improve the image contrast of CARS microscopy on nano-imaging.

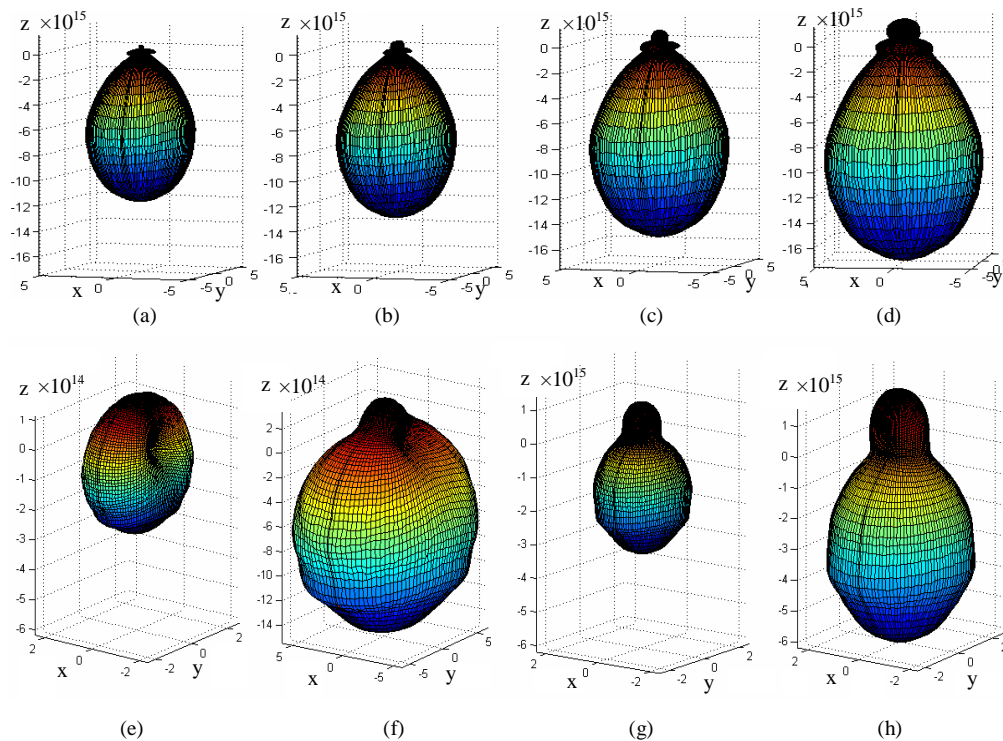


Fig. 4. The total scattering patterns from both the surrounding water and the nanoparticle with diameters of (a) 75 nm; (b) 125 nm; (c) 250 nm, and (d) 325 nm, respectively. (e), (f), (g), and (h) represent the scattering patterns from the nanoparticle alone with diameters of 75 nm; 125 nm; 250 nm, and 325 nm, respectively. Note that in z-axis, the negative values stand for CARS intensities in the forwarding scattering, whereas the positive values correspond to CARS intensities in the backward scattering.

As illustrated in Fig. 3, the intensity distributions of the light fields inside the particle and outside the particle (i.e., in the surrounding water) are different, and vary with particle sizes, and thus the corresponding light scatterings will also change with different particle sizes. Figure 5 shows the comparison of three different scatterings, i.e., the total scattering from both the nanoparticle and the surrounding water, the scattering from inside the nanoparticle, and the scattering from the surrounding water outside the nanoparticle, for (a) F-CARS and (b) E-CARS as a function of particle diameters. In F-CARS [Fig. 5(a)], the scattering from the smaller nanoscatterer is much weaker than that from the surrounding water outside the particle. Compared to the relatively constant scattering of surrounding water outside the particle, the scattering intensity from inside the particle rises rapidly with the increasing particle sizes. This suggests that in F-CARS imaging, the smaller nanoparticles appear to be dark spots, while the larger scatterers can be bright spots. As the detected scattering signals arise from the interference between the scatterings from the particles and the surrounding water outside the particles, and the latter only contributes to a relatively uniform nonresonant background, and thus the contrast of F-CARS image, to a certain extent, can be improved by subtraction to the relatively constant water background. In E-CARS [Fig. 5(b)], the scattering from the nanoscatterer is also weaker than that from surrounding water when the scatterer size is smaller than $\lambda_p/2$. However, with further increasing the particle size (larger than $\lambda_p/2$), the scattering from particles increases dramatically and dominates over the total scattering. The above results accord with the calculations shown in Fig. 3, whereby the local light field at the ‘virtual’ shell generated due to the near-field effect is much stronger than that inside the particle when the particle sizes are small, and thus the near-field enhanced scattering is stronger than that from the scatterer itself. Meanwhile, with further increasing the particle size (intensity profiles in Fig. 3), the electromagnetic field inside the scatterer and the excitation volume on the scatters increase rapidly, while the enhanced intensity at the ‘virtual’ shell structure (i.e., water-particle interface) drops off quickly with the increasing size, and hence the scattering from the surrounding water outside the particle becomes relatively weak.

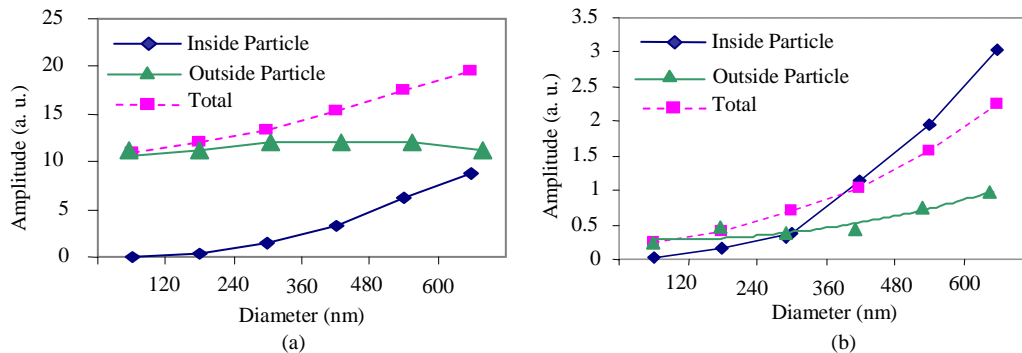


Fig. 5. Changes of scattering amplitudes as a function of particle diameters: (a) in F-CARS; and (b) in E-CARS. Note that the curve -■- corresponds to the total scattering from inside the particle and the surrounding water outside the particle, the curve -◆- stands for the scattering from inside the particle, and the curve -▲- stands for the scattering from the surrounding water outside the particle.

On the other hand, it is observed that the total-scattering is stronger than the scattering either from the surrounding water outside the particle or from inside the particle in forward direction [Fig. 5(a)], but in the backward scattering [Fig. 5(b)], this is true only when the particle size is smaller than $\lambda_p/2$. This phenomenon is due to the fact that the phase change occurs at the water-particle interface as shown in Fig. 3 (bottom panel). Owing to the refractive index mismatch ($\Delta n \sim 0.32$) at the nanoparticle-water interface, the maximum phase difference between the scatterings from the particle and the water can be $2\pi\Delta nd / \lambda_{\text{CARS}} + \varphi$ and $4\pi\Delta nd / \lambda_{\text{CARS}} + \varphi$ in the forward and backward scatterings, respectively. Where d is the diameter of the particle, and φ is the initial phase difference as shown in Fig. 3. As for the

forward scattering (F-CARS), the phase difference is always smaller than $\pi/2$, thereby resulting in a constructive interference of scatterings from the particles and the surrounding water for generating strong CARS. In the backward scattering (E-CARS), the phase difference can be smaller than $\pi/2$ for smaller particles (less than $\lambda_p/2$), thus the constructive interference between the small particles and the water can be established for generating a relatively high CARS signal. However, the phase difference in E-CARS can also be larger than $\pi/2$ for larger particles (larger than $\lambda_p/2$), resulting in a destructive interference for generating relatively small CARS signals [Fig. 5(b)].

3.5 Effect of the induced perpendicular polarization on CARS signals

To investigate the influence of nanoparticles on the polarization properties of the generated CARS signals, we calculated the distributions of the induced polarization of CARS in the focal volume of excitation light fields through a high NA, water objective, and compared the differences of polarization distributions between the two conditions: (1) from pure water, and (2) from nanoparticles with water.

Figures 6(a)-6(c) show the distribution of the induced polarization of water (without polystyrene beads) in the focal volume of the 0.9 N.A., water immersion objective in the x - y plane, whereby Figs. 6(a), 6(b), and 6(c) represent the distributions for x -component, z -component, and y -component, respectively. Obviously, the amplitude of the perpendicular component [y -component, Fig. 6(c)] is approximately 20 times weaker than that of the x -component [Fig. 6(a)], and this may be the main reason why the perpendicular polarization component was always neglected in most of CARS studies.

Figures 6(d)-6(f) show the distribution of the induced polarization of the 140 nm nanoparticle in water in the focal volume of the water objective in the x - y plane, whereby Figs. 6(d), 6(e), and 6(f) correspond to the distributions of x -component, z -component, y -component, respectively. Compared to the polarization distribution from pure water [Figs. 6(a) and 6(b)], there is only a relatively small change in the amplitudes of x - and z - components from nanoparticles [Figs. 6(d) and 6(e)]. However, the perpendicular component (i.e., y -component) of the induced polarization from nanoparticles [Fig. 6(f)] is found to be almost 6 times stronger than that from pure water [Fig. 6(c)]. Further calculations show that the enhancement of the perpendicular component only takes places in the regions at the particle-water interface and inside the particle. Therefore, with the advantages of the perpendicular polarization which is strictly confined to the nanoparticle-water interface, the perpendicular polarization CARS signal can be potentially useful for revealing the fine structures of living cells (e.g., membrane).

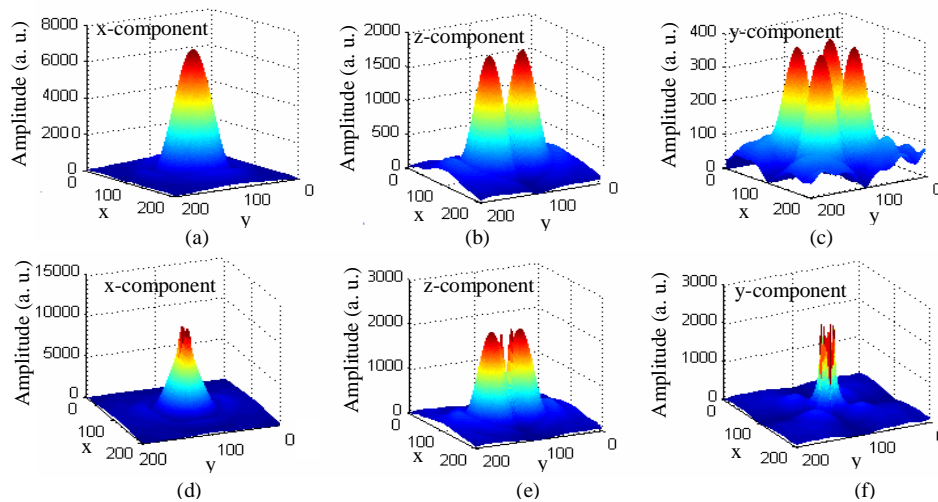


Fig. 6. Distribution of the induced polarization of the focal light fields on the x-y plane. (a), (b) and (c) represent the distribution for x-component, z-component, and y-component of pure water, respectively; (d), (e), and (f) correspond to the related distributions with 140 nm particles placed in the focal volume of a 0.9 N.A., water objective.

For a better understanding of how the induced perpendicular polarization contributes to the generated CARS signals, we compared the scattering from perpendicular component of the induced nonlinear polarization inside the nanoparticles with the total scattering and the scattering from the surrounding water outside the nanoparticle with different particle sizes in: (a) forward scattering direction, and (b) backward scattering direction, respectively (Fig. 7). In both forward and backward scatterings, the scattering of the perpendicular polarization component and the total scattering increase with increasing particle sizes. It is also observed that the total scattering is stronger than the scatterings either from the particle or from the surrounding water outside the particle in forward scattering, but the total scattering is weaker than the scattering from the water outside the particle in backward scattering [Fig. 7(b)]. This phenomenon is also due to the competition result of constructive and destructive interferences of the scatterings between the scatterers and the surrounding water.

Figure 7(c) shows the ratio of the induced perpendicular polarization component to the total scattering in both the forward and backward scatterings. Again, it confirms that the perpendicular polarization component only constitutes a very small fraction (less than 6%) of the total scattering in the forward direction. However, in backward scattering, the contribution of the perpendicular polarization component increases dramatically with the decreasing particle sizes. For example, the induced perpendicular polarization component for the 75 nm nanoparticles can contribute approximately 20% to the total scattering. Therefore, the contribution of perpendicular polarization component which is pertinent to the near-field effects should be taken into account for polarization CARS microscopy on nano-imaging.

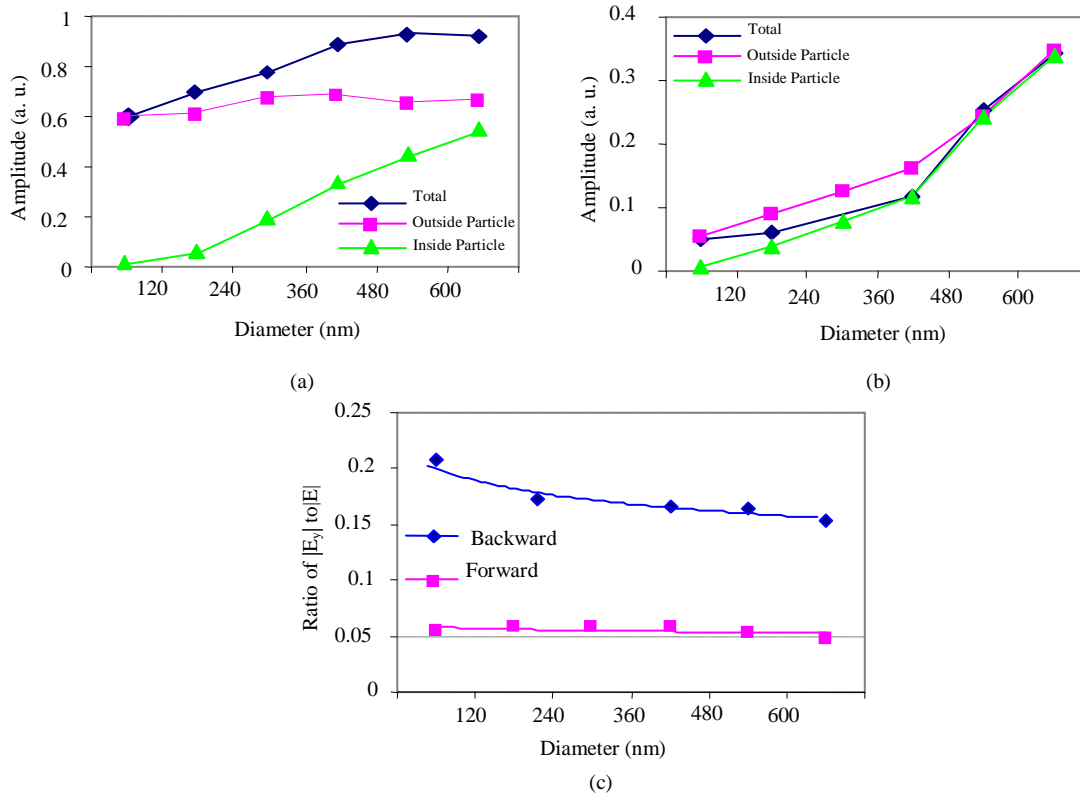


Fig. 7. Comparison of scattering amplitude of the induced perpendicular polarization component from nanoparticles with the total scattering and the scattering from surrounding water outside the nanoparticle: (a) in forward direction, and (b) in backward direction; (c) ratio of the perpendicular polarization component ($|E_y|$) to the total scattering ($|E|$) from nanoparticles in both forward and backward directions.

4. Discussion

In this study, we applied the advanced numerical method, FDTD, which bases on resolving the Maxwell equations directly with iterative strategy without the need of boundary conditions [14, 15], for the first time to study the near-field effects on CARS generation and propagation in nanoparticles. For the sake of simplicity but without losing the generality for CARS microscopy, the FDTD simulation model was developed to simulate the distributions of excitation light fields in the focal volume of the high N.A. water immersion objective, and the induced nonlinear polarization was calculated using the classic nonlinear formulas [1] associated with the simulated excitation light fields distribution, and then the scattering patterns of CARS signals from nanoparticles immersed in water are computed using the FDTD simulators. Although the literature has reported many analytical methods (e.g., the theory of angular spectrum representation, etc.) [22, 23] for studying the focused light field

distributions and scatterings in the excitation volume for microscopy, these analytical approaches are not efficient to deal with some objects or interfaces of interest, for example, the sub-wavelength-sized objects (e.g., cell membrane, nanometallic specimen) with irregular shapes or surfaces. The rough surface and index mismatching of sub-wavelength samples can lead to the evanescent wave generation and the surface plasmon generation at the interfaces between different media, and all these make the boundary conditions being extremely complex in the media. Thus it is difficult to directly derive the focal light field distributions and CARS generations of sub-wavelength-sized objects or interfaces using the existing analytical methods.

In E-CARS imaging on live cells [4], it is observed that the fine structures of small organelles (e.g., membrane) always appear to be relatively bright images with sharp edges as compared to other larger organelles in cells, and this phenomenon is usually considered as a result of higher backscatterings from smaller structures of cells. Our FDTD simulations on CARS scatterings from various sizes of nanoparticles indicate that near-field effects can also contribute a great deal to this phenomenon [Fig. 5(b)]. For the scatters with physical sizes of much less than the excitation light wavelength, due to the generations of evanescent waves by the near-field effect, the excitation light fields can be strongly enhanced especially at the scatterer-water interface, resulting in an additional highly localized excitation light field for CARS generation. This enhanced near-field excitation of CARS was found to be strictly confined to the scatterer-water interface, forming a 'virtual' shell structure surrounding the surface of the scatterer (Fig. 3). Simulation results also show that the CARS radiation from the virtual 'shell' structures can be much stronger than that from the nanoparticles, and it will become dominant in the backward scattering when the particle size is small than the half wavelength of excitation light [Fig. 5(b)]. These simulation results are in agreement with the observations of E-CARS experiments on cells or tissues [4].

The FDTD simulations also show that for the nanoparticle with a diameter of less than $\lambda_p/2$, the F-scattering is approximately 5 times stronger than the backward scattering in the perpendicular polarization direction, however, its F-scattering of parallel polarization is almost 20 times stronger than the corresponding backscattering (Fig. 5). This phenomenon is probably due to the different scattering volumes responsible for both parallel and perpendicular polarizations. In CARS experiments, both the scatterers and the surrounding solvent can radiate CARS signals in parallel polarization, thus the effective excitation volume is relatively large, leading to a large CARS radiation in parallel polarization. As most of total scattering energy is scattered in forward direction because of a relative large scattering volume (Fig. 4) or constructive interference with phase difference $<\pi/2$ (Fig. 3), this enables the forward scattering to be much stronger than that of backscattering. This coincides with most CARS experiments [5]. On the other hand, the perpendicular polarization component of CARS signals can be remarkably enhanced at the nanoparticle-water interface due to the near-field effect [Fig. 6(f)], and its back scattering can contribute almost 20% of the total scattering from particles if the particle size is in the order of tens of nanometers [Fig. 7(c)]. Since the induced perpendicular polarization by the near-field effect is strictly confined within the scatterers and the scatterer-water interface [Fig. 6(f)], the effective scattering volume of the surrounding water outside the particle is very small, thus it is expected that utilizing this perpendicular polarization component with less background interference from surrounding water will yield a good contrast of CARS image, and can also be useful for revealing the fine cellular structures in tissues and cells. One of the possible ways for separating the perpendicular component from other components (e.g., x-component) of the induced CARS polarization at the excitation volume can be realized by using a confocal scanning microscope system [24]. The confocal system can be used to illuminate the sample and collect the far-field CARS signal through a pinhole. By placing an analyzer/polarizer parallel to the y direction at the pinhole of the confocal microscope, the radiation field from the perpendicular component of the induced CARS polarization from the scatterer-water interface thus can be picked up selectively from other polarization components.

5. Conclusions

This study demonstrates that near-field effects can play an important role in CARS imaging. With the advantages of the perpendicular polarization which is strictly confined to the nanoparticle-water interface, the ratio polarization CARS imaging technique (i.e., ratio of scattering of perpendicular polarization to the total scattering) can be very useful for providing a high contrast of CARS image, and for revealing the fine structures of small organelles (e.g., membrane, mitochondrion) in live cells with nano-scale resolutions. One notes that although the FDTD model developed in this work is dedicated to CARS microscopy, it can be readily adapted to studying other nonlinear optical processes, such as two-photon/multi-photon microscopy, second and third harmonic generation microscopy, etc.

Acknowledgments

This work was supported by the Faculty Research Fund from National University of Singapore (NUS), the BioMedical Research Council, and the Academic Research Fund from Ministry of Education of Singapore.